metals

MDPI

Article

Morphology and Crystallography of Ausferrite in Austempered Ductile Iron

Chengduo Wang [1], Xueshan Du [1], Songjie Li [2,*], Yufu Sun [1] and Peixu Yang [1]

[1] School of Material Science and Engineering, Zhengzhou University, 100 Science Avenue, Zhengzhou 450001, China; wangchengduo@163.com (C.W.); duxueshan@zzu.edu.cn (X.D.); yufusun@zzu.edu.cn (Y.S.); yangpx@zzu.edu.cn (P.Y.)

[2] School of Chemical Engineering and Energy, Zhengzhou University, 100 Science Avenue, Zhengzhou 450001, China

* Correspondence: songjie@zzu.edu.cn; Tel.: +86-371-6388-7502

Received: 27 May 2017; Accepted: 26 June 2017; Published: 29 June 2017

Abstract: The microstructure of austempered ductile iron was investigated by electron backscatter diffraction technique. The results show that the orientation relationship between acicular bainitic ferrite and austenite is Greninger–Troiano relationship. A single austenite grain is divided into four packets and each packet contains six variants that share a $\{011\}_\alpha$ (i.e., $\{111\}_\gamma$) plane. When two γ grains are twinned, the twins share a $\{111\}_\gamma$ plane and have seven packets. The adjacent acicular bainitic ferrite plates (or laths) sharing a $\langle 001\rangle_\gamma$ axis have small misorientation of about 5.7°. The adjacent acicular bainitic ferrite plates (or laths) not sharing a $\langle 001\rangle_\gamma$ axis have two high misorientation angles of ~54.3° and ~60.0°. Further, the low angle boundary to high angle boundary ratio is far less than the ratio of the variant pairs with small misorientation to the ones with large misorientation. This work is available for structures obtained as a consequence of the heat treatment of austempering.

Keywords: electron backscatter diffraction; morphology; crystallography; acicular bainitic ferrite; austempered ductile iron

1. Introduction

Phase transformations strongly influence the microstructures of materials and, consequently, their mechanical properties [1–3]. During martensitic or bainitic transformation, the product phases keep specific crystallographic orientation relationships with the parent phases, which plays a crucial role in the nucleation and growth of transformed products and thus their morphology [4–6]. The orientation relations between parent austenite (γ) and transformed products are denoted as Kurdjumov–Sachs (K–S) [7], Nishiyama–Wassermann (N–W) [8,9], Greninger–Troiano (G–T) [10], Pitsch [11], and G–T′ (inverse G–T) [4] relations. In irons and steels, the orientation relationship is generally described as K–S or N–W relations [12–20]. Sometimes the orientation relationship between γ and martensite is characterized as the G–T relationship [21–24], which is generally considered to be intermediate [24–26] between K–S relation and N–W relation although the $\{111\}_\gamma$ plane is not exactly parallel to the $\{110\}_\alpha$ plane in G–T relation. However, the G–T relationship of bainite has not been found in irons and steels except low-carbon, high-alloy steel [25]. The Pitsch and N–W are two complementary orientation relations (the parallel planes and directions of martensite and those of γ are interchanged). The G–T and G–T′ are also complementary to each other.

Austempered ductile iron (ADI) is increasingly being used as a structural material due to its combination of high strength, toughness, and good wear resistance with low cost [27–32]. The attractive properties of ADI are related to its unique matrix that consists of acicular (bainitic) ferrite (α) and retained austenite, which is often referred to as "ausferrite" [30–32]. Actually, three-dimensional morphology of acicular bainitic ferrite is a plate or a lath [33]. Until now, the morphology of ausferrite

is generally analyzed by optical microscopy (OM) or scanning electron microscopy (SEM), which is deficient in the detailed knowledge of the morphological feature. More importantly, the orientation relationship between γ and α in ADI has not been well understood. The electron backscatter diffraction (EBSD) technique can provide detailed images of crystal morphology via a color-coded mapping of crystallographic orientation at each pixel. The aim of the present study is to investigate the morphological and crystallographic features of ausferrite in austempered ductile iron by an EBSD approach.

2. Materials and Methods

The ADI used in the present investigation has a chemical composition of 3.6C–2.7Si–1.3Mn–0.6Cu–0.6Cr–Fe balance (in wt %). The material was melted in a medium-frequency induction furnace (Zhengzhou Coal Mining Machinery, Zhengzhou, China). The melt was nodulized with 1.6 wt % $FeSiMg_8RE_3$ alloy, followed by innoculation with 1.3 wt % $FeSi_{75}$ alloy. Then, the melt was poured into sand molds in the form of Y-blocks according to the GB/T 24733-2009 [34]. The samples for isothermal heat treatment were machined from the Y-blocks. The austempering heat treatment process consists of austenitizing the samples at 900 °C for 90 min to get a full austenite matrix, and then quenching them at 270 °C for 90 min in a salt bath. After being withdrawn from the salt bath, the samples were air cooled to room temperature.

Specimens of 10 mm × 10 mm × 3 mm were machined from the heat-treated samples and polished to obtain a damage-free surface suitable for the EBSD measurements. The procedure was described in detail elsewhere [35]. The microstructure was examined using EBSD in a FE-SEM instrument (Zeiss LEO 1550, Zeiss, Oberkochen, Germany) equipped with the TexSEM Laboratories (TSL) system. The microscope was operated at an accelerating voltage of 20 kV and working distance of about 15 mm. The EBSD scans used a step size of 0.15 μm. The data was cleaned using the grain dilation provided by the TSL software (DJ Dingley, Salt Lake, UT, USA) and points with a confidence index (CI) of <0.02 were omitted. The experimental pole figures overlaid with the theoretical ones were created by rotating the experimental data. After the experimental data are rotated, the correspondence between the image and the pole figures is lost and the habit planes are no longer indexed.

3. Results

3.1. Analysis of Ferrite/Austenite

The inverse pole figure (IPF) orientation map of ausferrite in the ADI is shown in Figure 1a. The IPF orientation maps of the acicular bainitic ferrite and retained austenite in Figure 1a are shown in Figure 1b,c, respectively. The phase map of the ausferrite is shown in Figure 1d. From Figure 1a–d, it can be seen that the ausferrite mainly consists of acicular bainitic ferrite with a little retained austenite. All the α grains do not straddle the grain boundaries of prior austenites except a few of them (e.g., the α grain circled in Figure 1b) crossing the straight one (the twin boundaries). Clearly, refining prior austenite is an effective way of refining acicular bainitic ferrite.

In irons and steels, the orientation relationship between γ and α is generally described as K–S or N–W relations. The G–T relationship of bainitic ferrite has not been found in irons and steels except a low-carbon, high-alloy steel [25]. The G–T relationship can be conveniently approximated in terms of the following directions [4]: $\{111\}_\gamma$ // $\{011\}_\alpha$, $\langle 51217\rangle_\gamma$ // $\langle 71717\rangle_\alpha$.

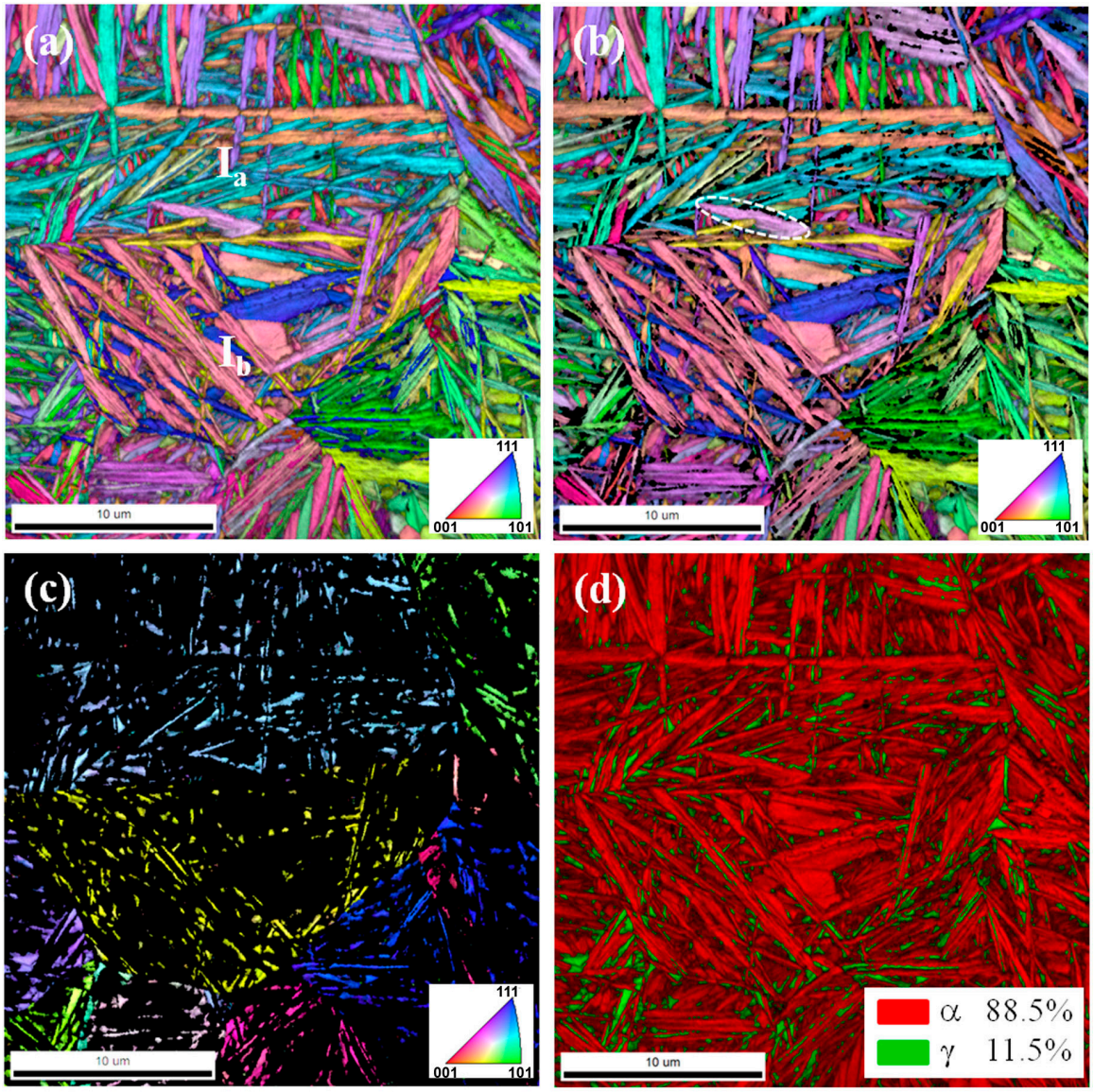

Figure 1. (**a**) Inverse pole figure (IPF) orientation map combined with image quality (IQ) map of ausferrite; (**b**) IPF orientation map combined with IQ map of the acicular bainitic ferrite in (**a**); (**c**) IPF orientation map combined with IQ map of the retained austenite in (**a**); (**d**) phase map of the ausferrite in (**a**). Prior γ grain I_a and I_b is labeled in (**a**). The α grain circled in (**b**) crossing the straight one (the twin boundaries).

Table 1 gives the 24 G–T variants keeping $(011)_\alpha$ parallel to $(1\,\bar{1}\,1)_\gamma$ or $(1\,1\,\bar{1})_\gamma$. The six G–T variants on the same close-packed planes of austenite form a packet. For example, the variants from GT1 to GT6 on the γ close-packed planes $(1\,\bar{1}\,1)_\gamma$ form one packet (denoted as P1). A prior γ grain can be divided into four packets because there are four close-packed planes $((111)_\gamma$, $(\bar{1}\,1\,1)_\gamma$, $(1\,\bar{1}\,1)_\gamma$, and $(1\,1\,\bar{1})_\gamma)$ in it. Furthermore, each $\langle 001\rangle_\gamma$ axis in a packet is shared by two variants, e.g., X is shared by GT1 and GT2. The two variants sharing a $\langle 001\rangle_\gamma$ axis in a packet (denoted as Bain paired variants) are misoriented by low angles of about 5.7°.

Table 1. The 24 G–T variants keeping $(011)_\alpha$ parallel to $(1\,\bar{1}\,1)_\gamma$ or $(1\,1\,\bar{1})_\gamma$.

G–T Variant	$\{111\}_\gamma$	$\{011\}_\alpha$	$\langle 51217\rangle_\gamma$	$\langle 71717\rangle_\alpha$	Bain Variant	Packet
GT1	$(1\,\bar{1}\,1)$	$(0\,1\,1)$	$[\bar{1}7\,\bar{5}\,12]$	$[\bar{7}\,\bar{1}7\,17]$	X	P1
GT2	$(1\,\bar{1}\,1)$	$(0\,1\,1)$	$[\bar{1}7\,\bar{1}2\,5]$	$[\bar{7}\,17\,\bar{1}7]$	X	
GT3	$(1\,\bar{1}\,1)$	$(0\,1\,1)$	$[12\,17\,5]$	$[\bar{7}\,\bar{1}7\,17]$	Y	
GT4	$(1\,\bar{1}\,1)$	$(0\,1\,1)$	$[5\,17\,12]$	$[\bar{7}\,17\,\bar{1}7]$	Y	
GT5	$(1\,\bar{1}\,1)$	$(0\,1\,1)$	$[5\,\bar{1}2\,\bar{1}7]$	$[\bar{7}\,\bar{1}7\,17]$	Z	
GT6	$(1\,\bar{1}\,1)$	$(0\,1\,1)$	$[12\,\bar{5}\,\bar{1}7]$	$[\bar{7}\,17\,\bar{1}7]$	Z	
GT7	$(1\,1\,\bar{1})$	$(0\,1\,1)$	$[\bar{1}7\,5\,\bar{1}2]$	$[\bar{7}\,\bar{1}7\,17]$	X	P2
GT8	$(1\,1\,\bar{1})$	$(0\,1\,1)$	$[\bar{1}7\,12\,\bar{5}]$	$[\bar{7}\,17\,\bar{1}7]$	X	
GT9	$(1\,1\,\bar{1})$	$(0\,1\,1)$	$[12\,\bar{1}7\,\bar{5}]$	$[\bar{7}\,\bar{1}7\,17]$	Y	
GT10	$(1\,1\,\bar{1})$	$(0\,1\,1)$	$[5\,\bar{1}7\,\bar{1}2]$	$[\bar{7}\,17\,\bar{1}7]$	Y	
GT11	$(1\,1\,\bar{1})$	$(0\,1\,1)$	$[5\,12\,17]$	$[\bar{7}\,\bar{1}7\,17]$	Z	
GT12	$(1\,1\,\bar{1})$	$(0\,1\,1)$	$[12\,5\,17]$	$[\bar{7}\,17\,\bar{1}7]$	Z	
GT13	$(\bar{1}\,1\,1)$	$(0\,1\,1)$	$[17\,5\,12]$	$[\bar{7}\,\bar{1}7\,17]$	X	P3
GT14	$(\bar{1}\,1\,1)$	$(0\,1\,1)$	$[17\,12\,5]$	$[\bar{7}\,17\,\bar{1}7]$	X	
GT15	$(\bar{1}\,1\,1)$	$(0\,1\,1)$	$[\bar{1}2\,\bar{1}7\,5]$	$[\bar{7}\,\bar{1}7\,17]$	Y	
GT16	$(\bar{1}\,1\,1)$	$(0\,1\,1)$	$[\bar{5}\,\bar{1}7\,12]$	$[\bar{7}\,17\,\bar{1}7]$	Y	
GT17	$(\bar{1}\,1\,1)$	$(0\,1\,1)$	$[\bar{5}\,12\,\bar{1}7]$	$[\bar{7}\,\bar{1}7\,17]$	Z	
GT18	$(\bar{1}\,1\,1)$	$(0\,1\,1)$	$[\bar{1}2\,5\,\bar{1}7]$	$[\bar{7}\,17\,\bar{1}7]$	Z	
GT19	$(1\,1\,1)$	$(0\,1\,1)$	$[17\,\bar{5}\,\bar{1}2]$	$[\bar{7}\,17\,\bar{1}7]$	X	P4
GT20	$(1\,1\,1)$	$(0\,1\,1)$	$[17\,\bar{1}2\,\bar{5}]$	$[\bar{7}\,\bar{1}7\,17]$	X	
GT21	$(1\,1\,1)$	$(0\,1\,1)$	$[\bar{1}2\,17\,\bar{5}]$	$[\bar{7}\,17\,\bar{1}7]$	Y	
GT22	$(1\,1\,1)$	$(0\,1\,1)$	$[\bar{5}\,17\,\bar{1}2]$	$[\bar{7}\,\bar{1}7\,17]$	Y	
GT23	$(1\,1\,1)$	$(0\,1\,1)$	$[\bar{5}\,\bar{1}2\,17]$	$[\bar{7}\,17\,\bar{1}7]$	Z	
GT24	$(1\,1\,1)$	$(0\,1\,1)$	$[\bar{1}2\,\bar{5}\,17]$	$[\bar{7}\,\bar{1}7\,17]$	Z	

The orientation relationship between γ and α can be examined by qualitative and quantitative procedures [15]. Here, we qualitatively identify the orientation relationship by comparing the ideal (011) pole figure with the measured one from EBSD. Figure 2a shows the gray-scale (011) pole figure of the acicular bainitic ferrite in prior γ grain I_a (labeled in Figure 1a) projected onto the $(111)_\gamma$ plane, with the poles from the ideal G–T relation of a single γ grain superimposed on it. The four packets in the ideal pole figure are expressed using green, violet, gold, and red colors. As can be seen, most of the experimental poles agree well with the theoretical ones. The K–S and G–T relations are quite similar to each other, so we have also superimposed an ideal K–S pole figure on the poles of the acicular bainitic ferrite in prior γ grain I_a to test whether the orientation relation is exactly a G–T or K–S relation, as shown in Figure 2b. Clearly, the experimental data is not well fit by the K–S relationship. Of course, the experimental data is also far away from the N–W relation which only has the half of G–T variants and much less poles. Though the G–T' relation cannot be distinguished from the G–T using commercial EBSD software such as TSL, it usually appears in precipitates [4]. Therefore, we think the orientation relationship between α and γ is the G–T relationship.

The packets within an austenite grain can be identified by highlighting the regions in which the variants share a common close-packed plane. The highlighted (011) pole figure and the corresponding packets for the prior γ grain I_a are presented in Figure 2c,d, respectively. In Figure 2c, the poles sharing a common close-packed plane are tinted in green, violet, gold, and red, respectively. Therefore, each color stands for one packet. Note that each rosette of poles is focused by the poles of one particular packet, indicating that the $\langle 001\rangle_\alpha$ axis is shared by the acicular bainitic ferrite plates (or laths) in the packet. The four $\langle 011\rangle_\alpha$ axes of the four packets are perpendicular to the $\{011\}_\alpha$ planes and correspond to the four $\langle 111\rangle_\gamma$ directions in the prior γ grain (normal to the four $\{111\}_\gamma$ planes). This means that the six variants in a particular packet share a common $\{011\}_\alpha$ (i.e., $\{111\}_\gamma$) plane. From Figure 2d, it can also be seen that there are four packets in I_a, which are highlighted in green (P1), violet (P2),

gold (P3), and red (P4), respectively. Further, any packet (P1, P2, P3, or P4) is subdivided into several disconnected areas.

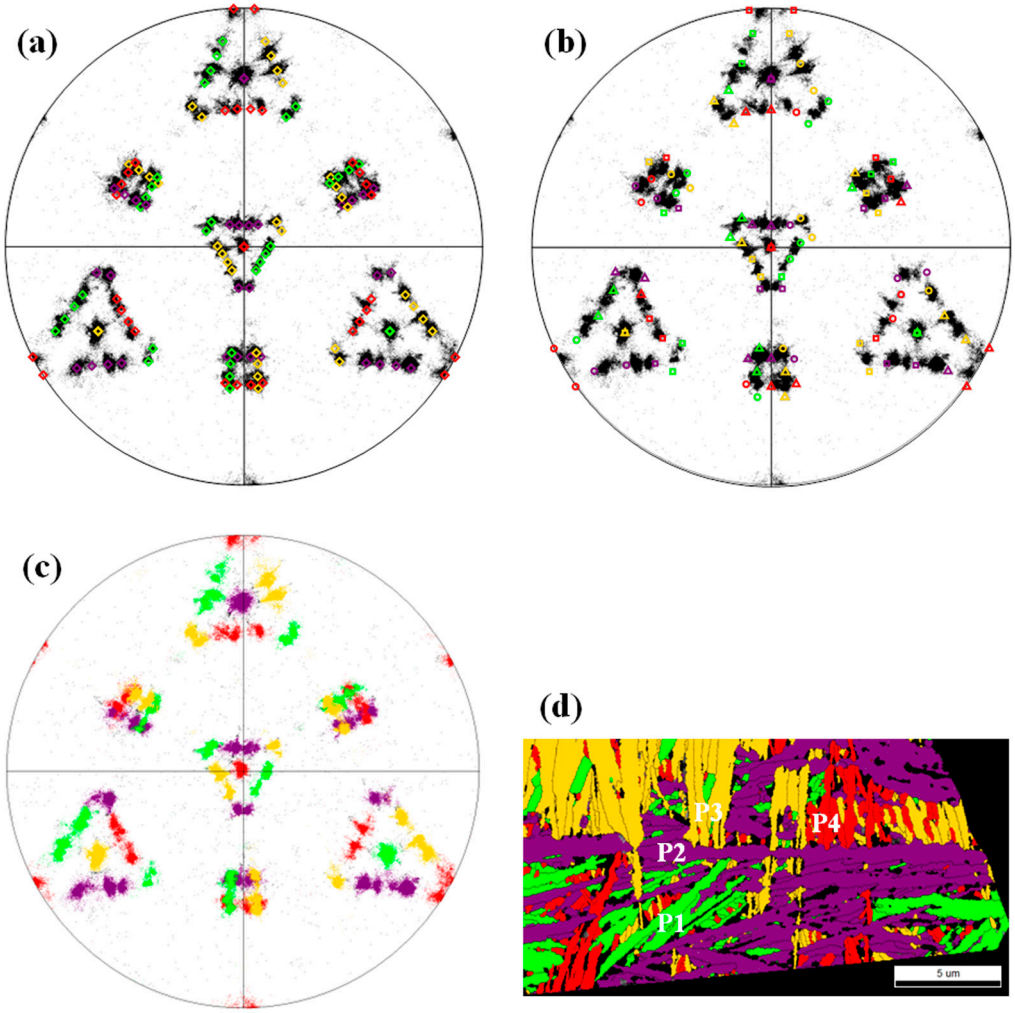

Figure 2. Gray-scale (011) pole figure of the acicular bainitic ferrite in prior γ grain I_a (labeled in Figure 1a) compared with the ideal pole figure for (**a**) the G–T relationship and (**b**) the K–S relationship, (**c**) (011) pole figure of the acicular bainitic ferrite in γ grain I_a colored to show the packets, and (**d**) corresponding packet map of the acicular bainitic ferrite. Black lines in (**d**) show the boundaries with misorientation angles larger than 10°. Each color stands for one packet.

It is noted that the grain boundary between the prior γ grains I_a and I_b (white dotted line) is very straight, as shown in the highlighted map of the retained austenite (Figure 3a). This means that the prior γ grains I_a and I_b could be twins. Figure 3b presents the highlighted (111) pole figure of the retained austenite in Figure 3a. It is apparent that the prior γ grains I_a and I_b are really twins and the twinning plane (twin boundary) is $(1\,1\,\bar{1})_\gamma$. In order to investigate the bainitic transformation of twinned austenite, the highlighted (011) pole figure and the corresponding packets of the acicular bainitic ferrite in I_a and I_b are displayed in Figure 3c,d, respectively. Note that the data were rotated. In Figure 3c, the poles of the acicular bainitic ferrite in I_a and I_b are pigmented in seven colors (green, violet, gold, red, pink, brown, and blue) with each color representing one packet. Clearly, there are seven packets in I_a and I_b. Further, we can see that there are two sets of pole figures with each similar to the calculated one, and the "violet" rosette (circled in Figure 3c) is shared by them. The shared rosette (shared packet) make the total number of the packets in I_a and I_b be one less than that it should be (eight), being the same as the previous results [24,36]. As mentioned above, each rosette of poles is

concentrated by the poles of one particular packet and the six variants in one packet share a $\{011\}_\alpha$ (i.e., $\{111\}_\gamma$) plane. The "violet" rosette means that the six variants in the "violet" packet share the $(011)_\alpha$ plane (violet color corresponds to the packet of P2 listed in Table 1). Therefore, the two sets of poles share the $(011)_\alpha$ (i.e., $(1\,1\,\bar{1})_\gamma$) plane. The colors in Figure 3d correspond to those in Figure 3c. From Figure 3d, it can be seen that the three packets highlighted in green, gold, and red lie in I_a, and the three packets highlighted in pink, brown, and blue lie in I_b. However, the "violet" packet lies both in I_a and I_b.

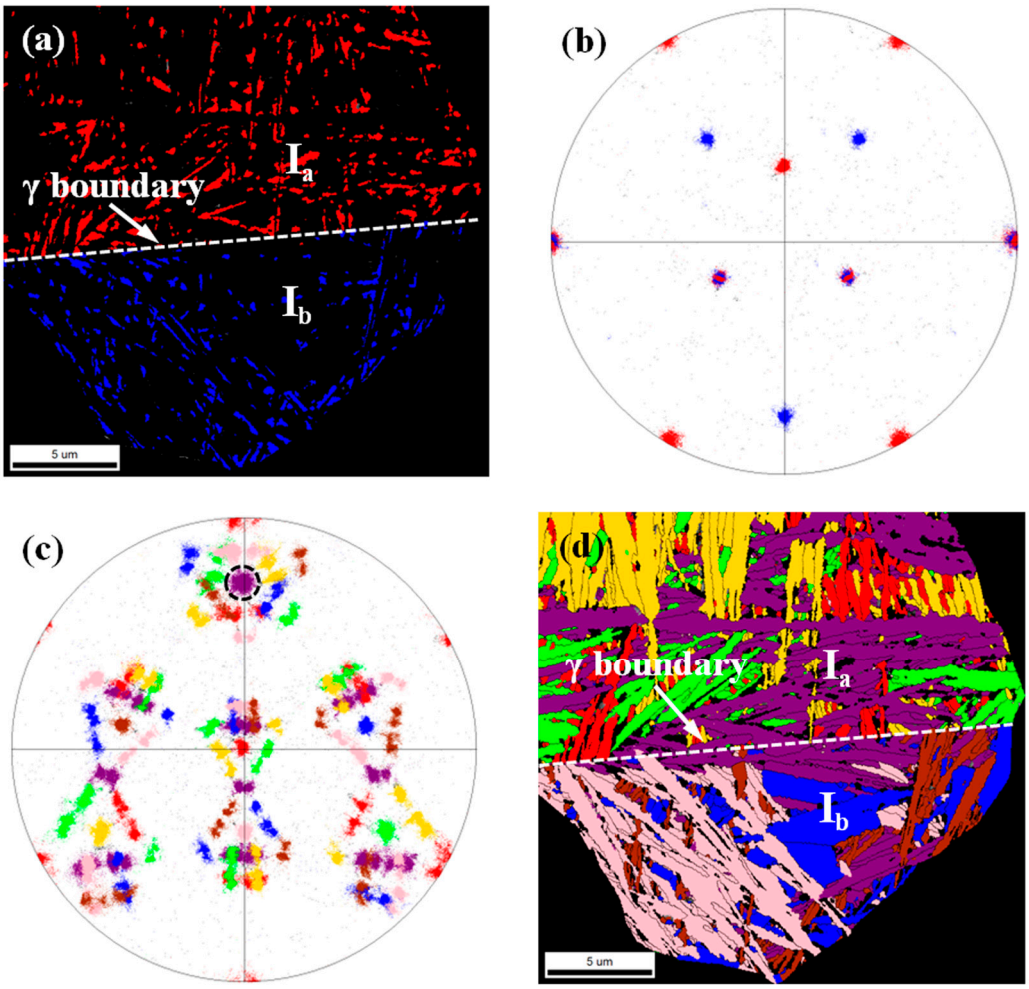

Figure 3. (**a**) Highlighted orientation map of the retained austenite in prior γ grains I_a and I_b, (**b**) (111) pole figure of the retained austenite in (**a**) colored to show the twins, (**c**) (011) pole figure of the acicular bainitic ferrite in γ grains I_a and I_b colored to show the packets, (**d**) corresponding packet map of the acicular bainitic ferrite. Black lines in (**d**) show the boundaries with misorientation angles larger than 10°. Each color stands for one packet.

In order to reveal the orientations of each acicular bainitic ferrite plates (or laths), we have re-colored the (011) pole figures of the "green" packet (P1) and the "violet" packet (P2) in Figure 2b, as shown in Figure 4a,c. The six variants within one packet (e.g., GT1, GT2, GT3, GT4, GT5, and GT6) are identified by six colors, with dark and light of the same color used for the Bain paired variants (e.g., GT1 and GT2). The pole figures show that the three Bain variant pairs of one packet colored in cyan, olive, and magenta (e.g., B1, B2, and B3) have significantly distinct orientations (a mean rotation of 120° (equivalently, of 60°)). Moreover, the orientation angles between the variants sharing a $\langle 001 \rangle_\gamma$ axis are less than 6°. Figure 4b,d display the highlighted acicular bainitic ferrite plates (or laths) of

the "green" packet (P1) and the "violet" packet (P2), respectively. Clearly, the six variants in a packet (e.g., GT1, GT2, GT3, GT4, GT5, and GT6) are present. Some of the six variants in a packet are adjacent to each other, but the others are disconnected. Further, the included angle between the adjacent acicular bainitic ferrite plates (or laths) sharing a $\langle 001 \rangle_{\gamma}$ axis is about 30° (as shown in the red circle of Figure 4b and the blue circle of Figure 4d). However, the misorientation angles between them are about 5.7°, as shown in Figure 5.

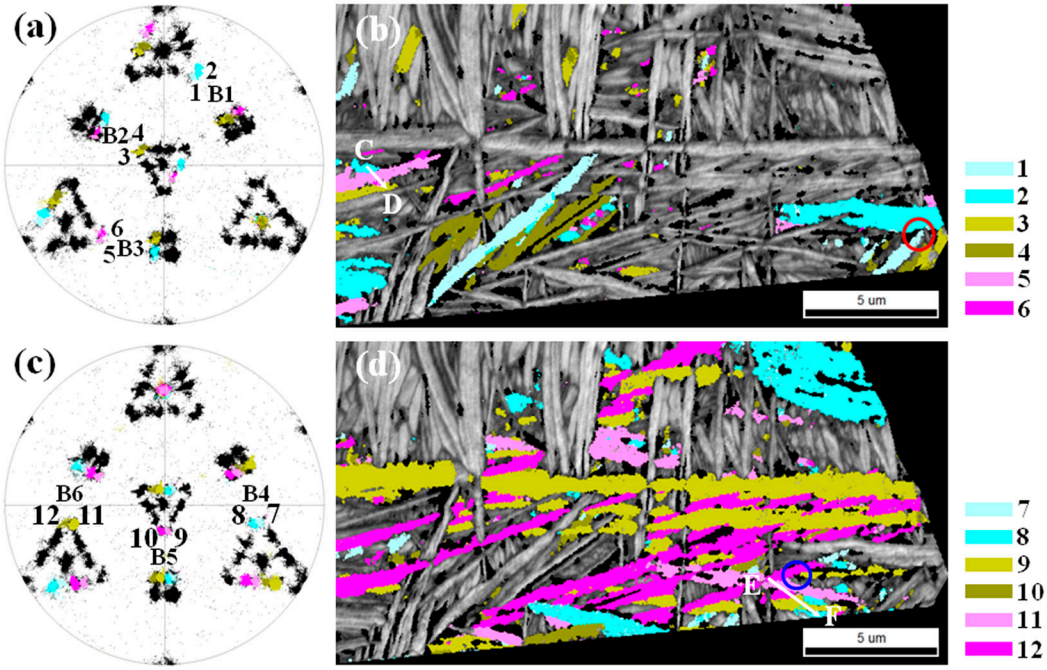

Figure 4. (**a**) (011) pole figure colored to show the acicular-ferrite orientations of the "green" packet (P1) in Figure 2b, (**b**) highlighted acicular-ferrite structure of the "green" packet (P1), (**c**) (011) pole figure colored to show the acicular-ferrite orientations of the "violet" packet (P2), (**d**) highlighted acicular-ferrite of the "violet" packet (P2). The variant names are further abbreviated as number, e.g., GT1 is abbreviated as 1. The B1, B2, B3, B4, B5, and B6 are the Bain variant pairs in (**a**,**c**). The lines from C to D in (**b**) and from E to F in (**d**) show the paths of point-to-point misorientation in Figure 5. The included angles between the adjacent acicular bainitic ferrite plates in the red circle of (**b**) and blue circle of (**d**) are about 30°.

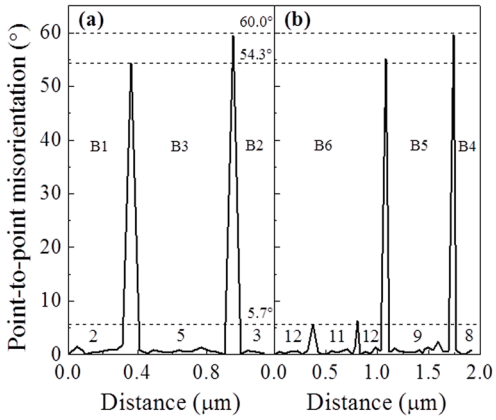

Figure 5. (**a**) Point-to-point misorientation along the line from C to D in Figure 4b, (**b**) point-to-point misorientation along the line from E to F in Figure 4d. B represents the Bain variant pairs, e.g., B1 stand for the "cyan" Bain variant pairs.

3.2. Ferrite/Austenite Boundaries

Figure 5a,b display the point-to-point misorientation along the line from C to D in the "green" packet (P1) of Figure 4b and the line from E to F in the "violet" packet (P2) of Figure 4d, respectively. Clearly, the adjacent acicular bainitic ferrite plates (or laths) which do not share a $\langle 001 \rangle_\gamma$ axis (e.g., GT2 and GT5, GT8 and GT9) have two misorientation angles of ~54.3°and ~60.0°. The adjacent acicular bainitic ferrite plates (or laths) sharing a $\langle 001 \rangle_\gamma$ axis (e.g., GT11 and GT12) have small misorientation of about 5.7°. These peak misorientation angles are close to the ideal values of 5.7°, 54.3°, and 60.0° calculated from the G–T relationship. We summarize three groups of the misorientation angles between adjacent variants in the "violet" packet (P2) and the number percentage of the variant pairs with the same misorientation in Table 2. Note that some variant pairs with the misorientation of 60° are twins, which have the twin misorientation of 54.3°/$[011]_\alpha$. For example, the misorientation angle of GT7-GT12 in the "violet" packet (P2) is 60°, but the twin misorientation between them is 54.3°/$[011]_\alpha$.

Table 2. The misorientation angles between adjacent variants in the "violet" packet (P2) and the number percentage of the variant pairs in the packet.

Group	Variant Pair	Misorientation Angle	Number Percentage
1	GT7-GT8, GT9-GT10, GT11-GT12	5.7°	20%
2	GT7-GT10, GT8-GT11, GT9-GT12	54.3°	20%
3	GT7-GT9, GT7-GT11, GT7-GT12 GT8-GT9, GT8-GT10, GT8-GT12 GT9-GT11, GT10-GT11, GT10-GT12	60°	60%

Figure 6 presents the boundary maps for the prior γ grain I_a. Here, we investigated the boundaries only based on misorientation larger than 3.5° because there is small misorientation less than 3.5° in acicular bainitic ferrite plates (or laths). From Figure 4, we can see that the length of red and black boundaries are 0.08 and 0.78 mm, respectively. This means that the boundary ratio of group 1 to group 2 + group 3 is about 1:10, which is far less than the ratio of the variant pairs in group 1 to the ones in group 2 + group 3 (1:4).

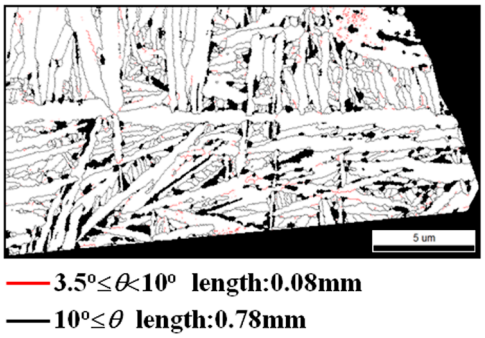

Figure 6. Boundary maps for the prior γ grain I_a.

4. Discussion

All the acicular bainitic ferrite grains do not straddle the grain boundaries of prior austenites. This means the fine acicular bainitic ferrite can be obtained if prior austenite is fine. Therefore, refining prior austenite is an effective way of refining acicular bainitic ferrite. The orientation relationship between acicular bainitic ferrite and austenite is the G–T relationship and the G–T variants form four packets in a single prior austenite. Each packet contains six G–T variants that share a $\{011\}_\alpha$ (i.e., $\{111\}_\gamma$) plane. Furthermore, the four packets interpenetrate and each is further divided into several disconnected areas in the two-dimension cross section. The three Bain variant pairs in one

packet have significantly distinct orientations (a mean rotation of 120° around the common $\langle 011 \rangle_\alpha$ axis), while the orientation angles between the variants sharing a $\langle 001 \rangle_\gamma$ axis are less than 6°.

The adjacent acicular bainitic ferrite plates (or laths) sharing a $\langle 001 \rangle_\gamma$ axis have small misorientation of about 5.7° around the common $\langle 011 \rangle_\alpha$ axis, but most of the included angle between them is about 30°. This means that most acicular bainitic ferrite plates or laths grow up along some specific crystal orientation. The adjacent acicular bainitic ferrite plates (or laths) not sharing a $\langle 001 \rangle_\gamma$ axis have two high misorientation angles of ~54.3° and ~60.0°. These values are close to the ideal values of 5.7°, 54.3°, and 60.0° calculated from the G–T relationship. However, the ratio of low angle boundary to high angle boundary (1:10) is far less than the ratio of the variant pairs with small misorientation to the ones with large misorientation (1:4). It has been found that the orientations inside some martensitic laths/plates gradually change and the continuous orientation impacts on the chances of variant contact [37]. Therefore, the low ratio of low angle boundary to high angle boundary could result from a continuum of orientations that exists between the low-angle misoriented variants. This means that the adjacent acicular bainitic ferrite plates or laths could be considered the basic element of austempered ductile iron.

5. Conclusions

All the acicular bainitic ferrite grains do not lie on the grain boundaries of prior austenites. The orientation relationship between acicular bainitic ferrite and austenite in our austempered ductile iron is a G–T relationship. A single austenite grain is divided into four packets, each of which contains six G–T variants that share a $\{011\}_\alpha$ (i.e., $\{111\}_\gamma$) plane. When two γ grains are twinned, the twins share a $\{111\}_\gamma$ plane and have seven packets. In a packet, the adjacent acicular bainitic ferrite plates (or laths) which do not share a $\langle 001 \rangle_\gamma$ axis have two high misorientation angles of ~54.3° and ~60.0°. The adjacent acicular bainitic ferrite plates (or laths) sharing a $\langle 001 \rangle_\gamma$ axis have small misorientation of about 5.7°, but most of the included angle between them is about 30°. Further, the low angle boundary to high angle boundary ratio is far less than the number percentage of the variant pairs with small misorientation to the ones with large misorientation. These results showed that the adjacent acicular bainitic ferrite plates or laths could be considered as the basic element of austempered ductile iron.

Acknowledgments: This work is supported in part by grants from the National Natural Science Foundation of China (Grant No. 51104136) and Key Scientific Research Projects of He'nan Educational Committee (No. 16A530003). These grants are gratefully acknowledged.

Author Contributions: Chengduo Wang and Songjie Li conceived and designed the experiments; Xueshan Du and Peixu Yang performed the experiments; Chengduo Wang and Xueshan Du analyzed the data; Yufu Sun contributed reagents/materials/analysis tools; Songjie Li wrote the paper.

Conflicts of Interest: The authors declare no conflict of interest.

References

1. Humbert, M.; Germain, L.; Gey, N.; Boucard, E. Evaluation of the orientation relations from misorientation between inherited variants: Application to ausformed martensite. *Acta Mater.* **2015**, *82*, 137–144. [CrossRef]
2. Guo, Z.; Lee, C.S.; Morris, J.W., Jr. On coherent transformations in steel. *Acta Mater.* **2004**, *52*, 5511–5518. [CrossRef]
3. Kitahara, H.; Ueji, R.; Tsuji, N.; Minamino, Y. Crystallographic features of lath martensite in low-carbon steel. *Acta Mater.* **2006**, *54*, 1279–1288. [CrossRef]
4. He, Y.; Godet, S.; Jonas, J.J. Observations of the Gibeon meteorite and the inverse Greninger–Troiano orientation relationship. *J. Appl. Cryst.* **2006**, *39*, 72–81. [CrossRef]
5. Morito, S.; Huang, X.; Furuhara, T.; Maki, T.; Hansen, N. The morphology and crystallography of lath martensite in alloy steels. *Acta Mater.* **2006**, *54*, 5323–5331. [CrossRef]
6. Sato, H.; Zaefferer, S. A study on the formation mechanisms of butterfly-type martensite in Fe–30% Ni alloy using EBSD-based orientation microscopy. *Acta Mater.* **2009**, *57*, 1931–1937. [CrossRef]
7. Kurdjumov, G.; Sachs, G. Über den mechanismus der stahlhärtung. *Z. Phys.* **1930**, *64*, 325–343. [CrossRef]

8. Nishiyama, Z. X-ray investigation of the mechanism of the transformation from face-centered cubic lattice to body-centered cubic. *Sci. Rep. Tohoku Univ.* **1934**, *23*, 637–664.
9. Wassermann, G. Uder den mechanismus der α-γ-umwandlung des eisens. *Verl. Stahleisen* **1935**, *17*, 149–155.
10. Greninger, A.B.; Troiano, A.R. The mechanism of martensite formation. *Met. Trans.* **1949**, *185*, 590–598.
11. Pitsch, W. The martensite transformation in thin foils of ironnitrogen alloys. *Philos. Mag.* **1959**, *4*, 577–584. [CrossRef]
12. Morito, S.; Tanaka, H.; Konishi, R.; Furuhara, T.; Maki, T. The morphology and crystallography of lath martensite in Fe–C alloys. *Acta Mater.* **2003**, *51*, 1789–1799. [CrossRef]
13. Ferry, M.; Xu, W. Microstructural and crystallographic features of ausferrite in as-cast gray iron. *Mater. Charact.* **2004**, *53*, 43–49. [CrossRef]
14. Zhang, S.; Morito, S.; Komizo, Y. Variant selection of low carbon high alloy steel in an austenite grain during martensite transformation. *ISIJ Int.* **2012**, *52*, 510–515. [CrossRef]
15. Miyamoto, G.; Iwata, N.; Takayama, N.; Furuhara, T. Quantitative analysis of variant selection in ausformed lath martensite. *Acta Mater.* **2012**, *60*, 1139–1148. [CrossRef]
16. Kinney, C.C.; Pytlewski, K.R.; Khachaturyan, A.G.; Morris, J.W., Jr. The microstructure of lath martensite in quenched 9Ni steel. *Acta Mater.* **2014**, *69*, 372–385. [CrossRef]
17. Furuhara, T.; Kawata, H.; Morito, S.; Maki, T. Crystallography of upper bainite in Fe–Ni–C alloys. *Mater. Sci. Eng. A* **2006**, *431*, 228–236. [CrossRef]
18. Pancholi, V.; Krishnan, M.; Samajdar, I.S.; Yadav, V.; Ballal, N.B. Self-accommodation in the bainitic microstructure of ultra-high-strength steel. *Acta Mater.* **2008**, *56*, 2037–2050. [CrossRef]
19. Takayama, N.; Miyamoto, G.; Furuhara, T. Effects of transformation temperature on variant pairing of bainitic ferrite in low carbon steel. *Acta Mater.* **2012**, *60*, 2387–2396. [CrossRef]
20. Suikkanen, P.P.; Cayron, C.; DeArdo, A.J.; Karjalainen, L.P. Crystallographic analysis of isothermally transformed bainite in 0.2C–2.0Mn–1.5Si–0.6Cr steel using EBSD. *J. Mater. Sci. Technol.* **2013**, *29*, 359–366. [CrossRef]
21. Shibata, A.; Murakami, T.; Morito, S.; Furuhara, T.; Maki, T. The origin of midrib in lenticular martensite. *Mater. Trans.* **2008**, *49*, 1242–1248. [CrossRef]
22. Kelly, P.M.; Jostsons, A.; Blake, R.G. The orientation relationship between lath martensite and austenite in low carbon, low alloy steels. *Acta Metall. Mater.* **1990**, *38*, 1075–1081. [CrossRef]
23. Pham, A.H.; Ohba, T.; Morito, S.; Hayashi, T. An advanced fitting method for crystallographic and morphological analyses of EBSD data applied for low-carbon steel martensite. *Mater. Trans.* **2013**, *54*, 1396–1402. [CrossRef]
24. Wang, C.; Qiu, H.; Kimura, Y.; Inoue, T. Morphology, crystallography, and crack paths of tempered lath martensite in a medium-carbon low-alloy steel. *Mater. Sci. Eng. A* **2016**, *669*, 48–57. [CrossRef]
25. Zhang, M.X.; Kelly, P.M. Accurate orientation relationship between ferrite and austenite in low carbon martensite and granular bainite. *Scr. Mater.* **2002**, *47*, 749–755. [CrossRef]
26. Qi, L.; Khachaturyan, A.G.; Morris, J.W., Jr. The microstructure of dislocated martensitic steel: Theory. *Acta Mater.* **2014**, *76*, 23–39. [CrossRef]
27. Hsu, C.-H.; Chuang, T.-L. Influence of stepped austempering process on the fracture toughness of austempered ductile iron. *Metall. Mater. Trans. A* **2001**, *32*, 2509–2513. [CrossRef]
28. Francucci, G.; Sikora, J.; Dommarco, R. Abrasion resistance of ductile iron austempered by the two-step process. *Mater. Sci. Eng. A* **2008**, *485*, 46–54. [CrossRef]
29. Han, C.F.; Wang, Q.Q.; Sun, Y.F.; Li, J. Effects of molybdenum on the wear resistance and corrosion resistance of carbidic austempered ductile iron. *Metallogr. Microstruct. Anal.* **2015**, *4*, 298–304. [CrossRef]
30. Yang, J.; Putatunda, S.K. Improvement in strength and toughness of austempered ductile cast iron by a novel two-step austempering process. *Mater. Des.* **2004**, *25*, 219–230. [CrossRef]
31. Erić, O.; Rajnović, D.; Zec, S.; Sidjanin, L.; Jovanović, M.T. Microstructure and fracture of alloyed austempered ductile iron. *Mater. Charact.* **2006**, *57*, 211–217. [CrossRef]
32. Elsayed, A.H.; Megahed, M.M.; Sadek, A.A.; Abouelela, K.M. Fracture toughness characterization of austempered ductile iron produced using both conventional and two-step austempering processes. *Mater. Des.* **2009**, *30*, 1866–1877. [CrossRef]
33. Wu, K.M. Three-dimensional analysis of acicular bainitic ferrite in a low-carbon steel containing titanium. *Scr. Mater.* **2006**, *54*, 569–574. [CrossRef]

34. GB/T 24733-2009. *Austempered Ductile Iron (ADI) Castings*; China Standard Press: Beijing, China, 2009.
35. Wang, C.; Qiu, H.; Inoue, T. Delaminating crack paths in ultrafine, elongated ferritic steel. *ISIJ Int.* **2009**, *53*, 2272–2274. [CrossRef]
36. Germain, L.; Gey, N.; Mercier, R.; Blaineau, P.; Humbert, M. An advanced approach to reconstructing parent orientation maps in the case of approximate orientation relations: Application to steels. *Acta Mater.* **2012**, *60*, 4551–4562. [CrossRef]
37. Cayron, C. EBSD imaging of orientation relationships and variant groupings in different martensitic alloys and Widmanstätten iron meteorites. *Mater. Charact.* **2014**, *94*, 93–110. [CrossRef]